

O₂ Physisorption in Coal Pore: Effects of Pore Size, Pressure, Temperature and Function Group

Gang Cheng

China University of Mining and Technology (Beijing) <https://orcid.org/0000-0003-3658-2076>

Bo Tan (✉ tanbo709@126.com)

China University of Mining and Technology (Beijing)

Shuhui Fu

China University of Mining and Technology (Beijing)

Feiran Wang

China University of Mining and Technology (Beijing)

S.I. : Control of Coal Fire

Keywords: Oxygen, Physisorption, GCMC, Coal pore

Posted Date: January 3rd, 2022

DOI: <https://doi.org/10.21203/rs.3.rs-1121077/v1>

License: © ⓘ This work is licensed under a Creative Commons Attribution 4.0 International License.

[Read Full License](#)

23 Coal resources in the mining, transportation, storage process is prone to coal spontaneous
24 combustion and thus cause fires[1], the annual loss due to coal fires as much as \$ 200 million[2]. The
25 problem of coal fires is becoming increasingly serious as coal resources increase in reserves[3]. The
26 initial stage of coal spontaneous combustion for mainly has oxygen diffusion into the pores of coal, and
27 the occurrence of physical and chemical adsorption on the surface of coal, thus causing the low-
28 temperature oxidation reaction of coal[4, 5]. Therefore, in order to prevent oxygen adsorption in the
29 pores of coal and to prevent spontaneous coal combustion at source, it is necessary to have a better
30 understanding of the physical adsorption properties of oxygen in the pores of coal.

31 Coal belongs to porous medium[6, 7], with the continuous development of coal the ratio of each
32 pore size in coal is constantly changing[8, 9], thus affecting the adsorption of various gases in
33 coal[10-12]. Scholars have investigated the adsorption characteristics of methane[13], carbon
34 dioxide[14], carbon monoxide[15], nitrogen[16] and other gases in coal pores by experimental tests and
35 molecular simulation methods. In particular, coalbed methane reserves and extraction had been studied
36 by scholars from the perspective of coal pore through the properties of coal[17], ambient
37 temperature[13], gas pressure[18], etc. With the improvement of computer technology and the
38 popularization of molecular simulation software, the adsorption behavior of single or multiple
39 gases[19-21] in coal pores had been analyzed by many researchers through the Grand Canonical Monte
40 Carlo (GCMC)[22, 23] and Density Functional Theory (DFT) methods[24, 25] used Materials studio[26],
41 Gaussian[27], VASP[28] and other software[29, 30], which included parameters such as adsorption
42 amount, heat of adsorption, adsorption force, equilibrium distance, etc. The adsorption characteristics
43 of various gases in coal pores were obtained. During the molecular simulation, it was found that there
44 were differences in the adsorption characteristics of gases depended on the pore size, group,

45 temperature, and pressure[13, 31], the reasons for these are also closely related to the size and
46 interaction potential energy of the gas molecules[14, 32-34]. At the same time, coal is a cross-linked
47 molecule with high molecular weight[7]. In order to simplify the molecular structure of coal, scholars
48 mostly adopted the graphite slit model with regular arrangement of carbon atoms to study the effect of
49 coal pore structure on gas adsorption, and the results obtained by molecular simulation showed good
50 similarity with the experimental results[35-37].

51 In the study of adsorption properties, the pore classification method proposed by Chinese scholar
52 Yidong Cai is mostly used: micropore (<2 nm), small pore (2-10 nm), medium pore (10- 10^2 nm), large
53 pore (10^2 - 10^3 nm), very large pore (10^3 - 10^4 nm), and microfracture ($>10^4$ nm)[38, 39]. According to
54 adsorption science, the gas adsorption behavior is influenced by the pore structure distribution
55 (PSD)[40], and the pore sizes responsible for these effects are mainly in micropores and
56 micropores[41], while adsorption in mesopores and macropores is not included in the overall gas
57 adsorption capacity[10]. Where the micropore filling effect causes gas adsorption in micropores and the
58 surface adsorption effect causes gas adsorption in small pores, and these were derived from a
59 comprehensive analysis of experiments and molecular simulations[42].

60 The literature studied on the adsorption characteristics of oxygen in the pore structure of coal was
61 few, and most of them derived the macroscopic effect of the coal pore structure on the oxygen
62 adsorption amount by experimental means, and did not reveal the mechanism of oxygen adsorption in
63 coal pores from the microscopic molecular level[43-48]. The effect of fractal dimension and pore
64 volume of the coal pore structure on the adsorption of oxygen by coal was revealed through our
65 previous work[12]. Meanwhile, Xianzhe Lv et al, used the pore-scale model has been developed by
66 employing the two-dimensional Sierpinski carpet model in order to study the oxygen adsorption

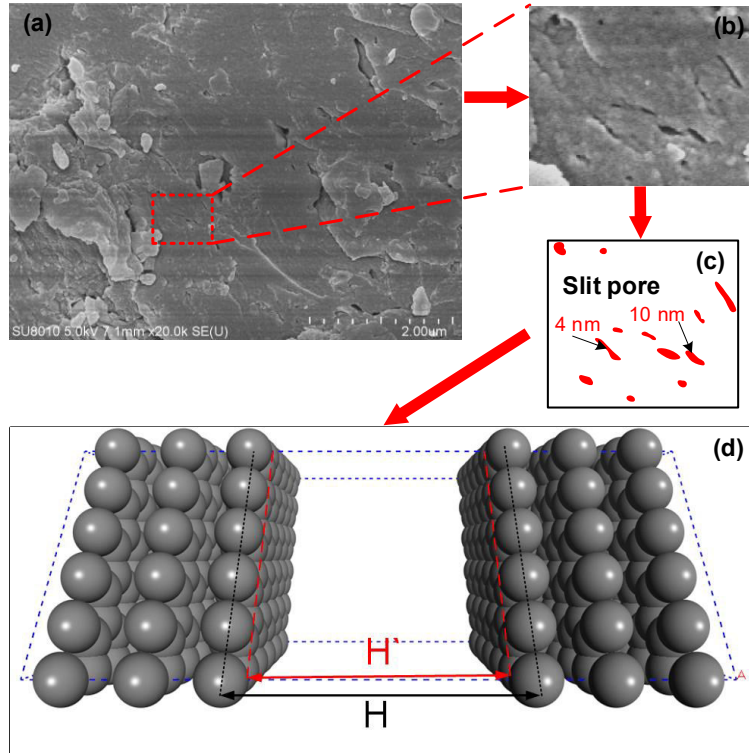
67 performance of coal porous media, which was constructed in this paper to model the pore size of coal,
68 mainly also the fractal dimension and permeability of coal[49]. Hai-hui Xin et al. also analyzed the
69 adsorption energy and charge changes between oxygen and each group by experimental and density
70 flooding methods to derive the adsorption sites[50].

71 Although researchers had studied the adsorption behavior of methane, carbon dioxide, nitrogen,
72 oxygen and other gases in coal pores, the adsorption characteristics of oxygen in coal pores under the
73 combined conditions of pore size, ambient temperature, atmospheric pressure and other parameters of
74 coal were still absent. And these are important for understanding the mechanism of oxygen adsorption
75 in coal and proposing reasonable and feasible preventive measures against spontaneous combustion of
76 coal. Therefore, in this paper, based on the assumption of no chemisorption, the physisorption
77 characteristics of oxygen in coal pores at the microscopic molecular level were derived by constructing
78 graphite slit models with sizes ranging from 0.4 to 5 nm at different temperature and pressure
79 conditions using the standard GCMC method and COMPASS force field.

80 **2 Models and simulation**

81 **2.1 Models**

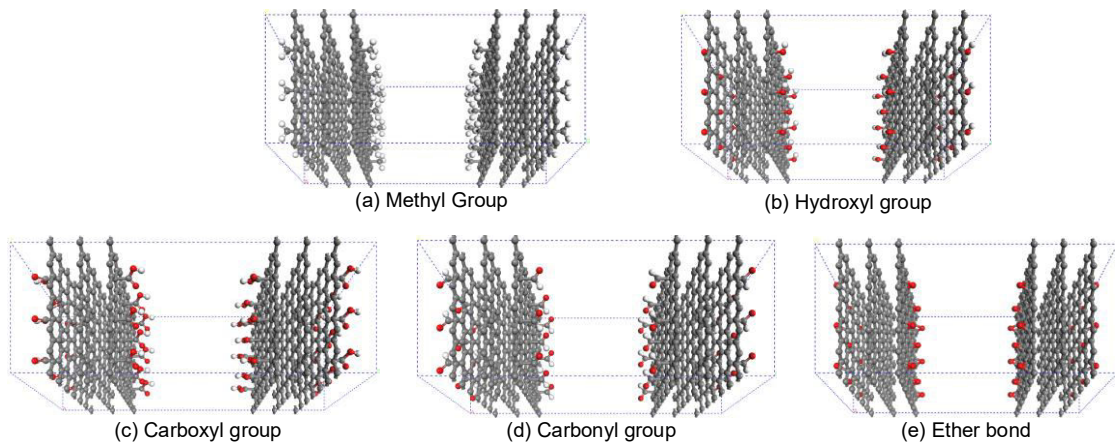
82 The most critical to simulate the adsorption characteristics of gases in coal is the reasonable
83 construction of molecular models. The numerous slit-type and round-type pore structures below 10 nm
84 diameter were found on the surface of coal (lignite from the Xilinhote region of Inner Mongolia, China)
85 by scanning electron microscopy (SEM) techniques, as shown in Figure 1 a-c. When studying the coal
86 pore structure on gas adsorption characteristics, the graphite slit model was often used[13, 31, 35, 37,
87 51], as shown in Figure 1 d.



88

89 Fig. 1 SEM image of coal sample (a), surface image of coal after local magnification of 300 times (b),
 90 representative nano-scale pores in the coal (c), graphite slit model (d).

91 However, coal molecules contain various types of groups made up of hydrogen and oxygen atoms
 92 in addition to carbon atoms in high content. As shown in Fig. 2, there were five models, which were
 93 methyl model (a), hydroxyl model (b), carboxyl model (c), carbonyl model (d), and ether bond model
 94 (e).



95

96

Fig. 2 Model of graphite slit pores modified by various groups

97 As in Figure 1(c), the default distance between graphite slit models in the molecular simulation
98 software was H , but the distance between the pore walls of coal in the actual case was H' , the
99 conversion equation between H and H' was as follows.

$$100 \quad H' = H - d_c \quad (1)$$

101 Where: d_c is the Carbon atomic diameter, 0.34 nm.

102 2.2 The details of simulation and calculation

103 The adsorption simulation was performed by GCMC method with graphite slit model as adsorbent
104 and oxygen molecules as adsorbate, and the *Metropolis* algorithm[52] was used during the simulation
105 to keep the chemical potential and volume stable. The total number of simulation steps was positioned
106 at 6.0×10^6 in order to achieve thermodynamic equilibrium in the adsorption simulation, with 3.0×10^6
107 equilibrium steps to ensure adsorption equilibrium and 3.0×10^6 production steps to capture the
108 accurate equilibrium steps.

109 Molecular dynamics simulations require the selection of a suitable force field for the calculation.
110 In this paper, we adopted the COMPASS force field, which can accurately and rapidly predict the
111 structural and thermophysical properties of organic matter and is widely used in the simulation of
112 coal-related products and their adsorption[16, 27, 29, 53, 54]. The composition of the molecular
113 potential energy is as follows.

$$E_{total} = E_{val} + E_{Non} \quad (2)$$

$$E_{val} = E_{Bo} + E_{An} + E_{Tor} + E_{In} \quad (3)$$

$$E_{Non} = E_{Van} + E_{elec} + E_{hy} \quad (4)$$

114 Where the total energy (E_{total}) is composed of the valence energy (E_{val}) and non-bond energy
115 (E_{Non}). The E_{Non} is constituted by energy of band (E_{Bo}), angel (E_{An}), torsion (E_{Tor}), and inversion (E_{In}),

116 while the E_{Val} is by energy of Van der Waals (E_{Van}), electrostatic (E_{elec}), and hydrogen bond (E_{hy}), the
 117 unit is KJ/mol.

118 The adsorption of coal molecules on oxygen by van der Waals forces. The van der Waals forces
 119 for non-bonding interactions between homogeneous or heterogeneous molecules in the COMPASS
 120 force field use the Lennard-Jones 9-6 potential energy equation[27]. The Lennard-Jones 9-6 potential
 121 energy equation is as follows.

$$E_{ij} = 4\varepsilon_{ij} \left[2 \left(\frac{r_{ij}^0}{r_{ij}} \right)^9 - 3 \left(\frac{r_{ij}^0}{r_{ij}} \right)^6 \right] \quad (5)$$

122 where E_{ij} is the Lennard-Jones potential energy, ε_{ij} is the potential energy trap parameter, r_{ij}^0 is the
 123 distance at which the potential energy is lowest, and r_{ij} is the distance between the two.

124 The potential energy of oxygen molecules with coal pore surfaces is calculated by the 10-4-3
 125 model[55]. The calculation formula is as follows.

$$A = [2\pi\sigma_{sf}^2\varepsilon_{sf}\rho\Delta] \quad (6)$$

$$\phi_{sf}(z) = A \left[\frac{2}{5} \left(\frac{\sigma_{sf}}{z} \right)^{10} - \left(\frac{\sigma_{sf}}{z} \right)^4 - \frac{\sigma_{sf}}{3\Delta(0.61\Delta + z)^3} \right] \quad (7)$$

126 Where: ρ is the number density of graphite, 114 nm^{-3} ; Δ is the distance between graphite layers,
 127 0.335 nm ; z is the distance between different molecules or atoms, nm ; σ_{sf} and ε_{sf} , are the potential
 128 energy parameters between different molecules or atoms, calculated by the Lorentz-Betherlot mixing
 129 rule[56] with the following equations. The Lennard-Jones potential energy parameters of oxygen
 130 molecules and carbon atoms are listed in Table 1.

$$\sigma_{sf} = (\sigma_{ff} + \sigma_{ss})/2 \quad (8)$$

$$\varepsilon_{sf} = \sqrt{\varepsilon_{ss}\varepsilon_{ff}} \quad (9)$$

131 Table 1 Oxygen molecules and carbon atoms adsorption potential energy parameters[57, 58]

Molecules	σ , nm	ε/k , K
O ₂	0.3467	106.7
C	0.3400	28.0

132 In the graphite slit model, both the upper and lower carbon atoms have an action potential with
 133 oxygen. Therefore, the total potential energy in the graphite slit model is the sum of the top and bottom
 134 potentials. The calculation formula is as follows.

$$\phi = \phi_{sf}(H) + \phi_{sf}(H - z) \quad (10)$$

135 The adsorption equilibrium system obtained by GCMC method simulates the presence of
 136 adsorbed-state gas and free-state gas, and the simulation results in the total adsorption gas amount of
 137 the adsorption system. The real amount of adsorbed-state gas should be the total adsorption gas amount
 138 minus the amount of free-state gas, and the amount of adsorbed gas is called excess adsorption gas [19,
 139 59, 60]. The calculation formula is as follows.

$$n_{ex} = n_{total} - V\rho_g \quad (11)$$

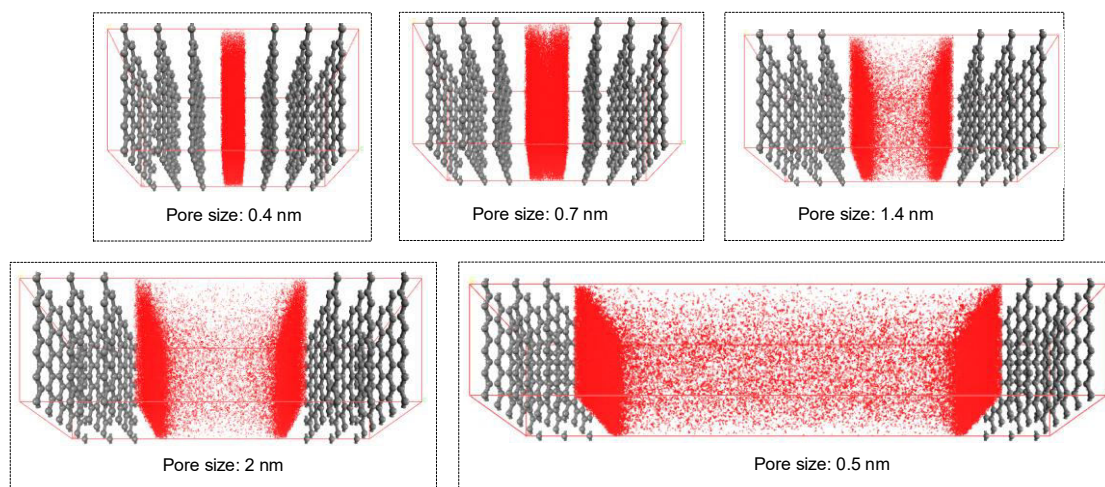
140 Where: n_{ex} is the excess adsorption amount; n_{total} is the total adsorption gas amount; V is the total
 141 volume of the adsorption system except for the adsorbent, the volume of the vacuum layer in the
 142 graphite slit model; ρ_g is the density of the gas phase, which can be calculated by the Peng-Robinson
 143 equation.

144 3 Results and Discussion

145 3.1 The distribution of intermolecular potential energy and oxygen density

146 Figure 3 shows the density distribution characteristics of oxygen in graphite slit pores of different
 147 pore sizes at 298 K and 0.1 MPa. When the pore size was 0.4 nm, there was only one adsorption layer
 148 because the van der Waals radius of oxygen molecules was 1.52 nm [61] and only one layer of oxygen

149 molecules could be accommodated in that pore. When the pore size was larger than 0.7 nm, there were
 150 two adsorption layers, while the amount of oxygen in the free-state in the graphite slit model kept
 151 increasing. While oxygen was basically physically adsorbed on the graphite surface in the form of a
 152 single layer at atmospheric pressure, when the pressure was increased after 6 MPa oxygen would form
 153 a double layer physically adsorbed on the graphite surface.
 154

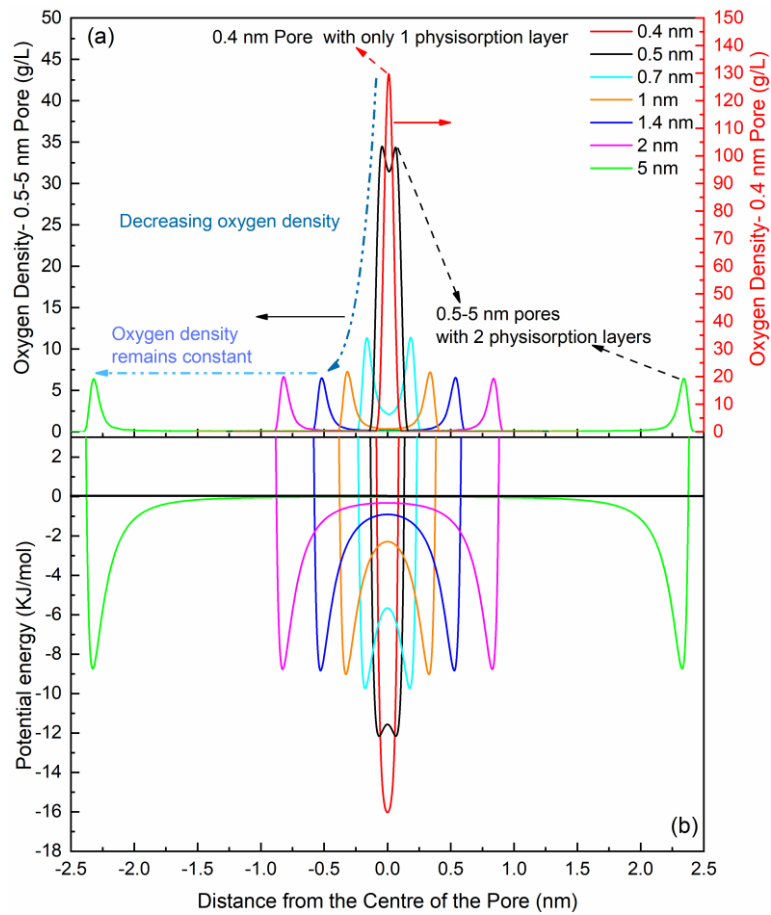


155
 156 Figure 3 Physisorption characteristics of oxygen in pores of different sizes (298 K/0.1 MPa). The red
 157 dots are the distribution density of oxygen, and the more dense red dots represent the higher oxygen
 158 density.

159 Figure 4(a) shown the density distribution of oxygen in graphite slit pores with different pore sizes
 160 at 298 K and 0.1 MPa, which more directly got to express the oxygen distribution in graphite slit pores.
 161 In the 0.4 nm pore, the higher density oxygen physisorption layer was only one layer and had a very
 162 high adsorbed state of oxygen (132.367 g/L), which was significantly greater than the density of
 163 oxygen in the other pores. In the pores from 0.5 to 5 nm, the higher density oxygen physisorption layer
 164 had two layers with the highest values of oxygen in the adsorbed state: 35.214 g/L (0.5 nm), 11.890 g/L
 165 (0.7 nm), 7.675 g/L (1 nm), 6.941 g/L (1.4 nm), 7.084 g/L (2 nm), 6.819 g/L (5 nm). The physisorption

166 density of oxygen decreases continuously in the 0.4-1 nm pores, while it remained essentially constant
167 after 1 nm.

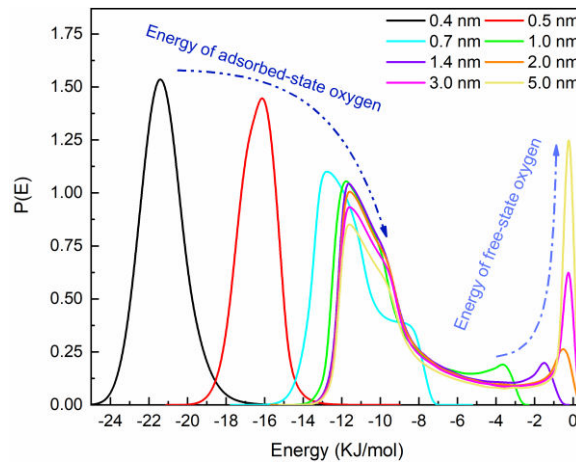
168 In general, the potential energy of interaction between gas molecules and coal pore surface affects
169 the adsorption characteristics of gas molecules on coal pore surface. Therefore, the potential energy of
170 the interaction between oxygen and the surface was calculated as in Figure 4(b) for different pore sizes
171 of the slit pores. When the physisorption reached dynamic equilibrium, the lowest point of potential
172 energy between the coal pore surface and oxygen tended to be the location with the highest density of
173 oxygen in the adsorbed-state, where the force between the coal pore surface and oxygen was the
174 highest. In the 0.4 nm pore, there was only one potential energy minimum (-16.05084 KJ/mol), so there
175 was only one layer of adsorbed-state oxygen in the 0.4 nm pore; in the 0.5-5 nm pore, there were two
176 potential energy minima each: -12.17272 KJ/mol (0.5 nm), -9.76817 KJ/mol (0.7 nm), -9.06885
177 KJ/mol (1 nm), -8.87821 KJ/mol (1.4 nm), -8.81643 KJ/mol (2 nm), and -8.79021 KJ/mol (5 nm). It
178 was obvious that the trend of potential energy change from 0.4 nm to 5 nm in the pores was similar to
179 the trend of oxygen density change.



180

181 Figure 4 Oxygen density distribution in different sized slit pores (298 K/0.1 MPa) (a). Intermolecular
 182 potential energy distribution in different sized slit pores (b).

183 The distribution of oxygen physisorption energy in coal pores of different sizes was inconsistent,
 184 which included the adsorption energy of oxygen molecules in the adsorbed-state (solid to gas) and the
 185 adsorption energy of oxygen molecules in the free-state (gas to gas). It could be seen that in the pores
 186 below 1.0 nm, only the adsorption energy of the adsorbed-state oxygen molecules was available, and
 187 the value and proportion of the physisorption energy was decreasing due to the potential energy. In the
 188 pores above 1.0 nm, the physisorption energy of the adsorbed-state oxygen molecules remained
 189 constant (12 KJ/mol) with the increasing of the pore size but the ratio kept decreasing, while the value
 190 and ratio of the adsorption energy of the free-state oxygen kept increasing.



191

192 Figure 5 Physisorption energy distribution of oxygen in graphite slits of different sizes (298 K/0.1

193 MPa)

194 3.2 Effect of pressure on the physisorption of oxygen in different size pores

195 Figure 6(a) shown the excess oxygen physisorption at 298 K for different pore sizes (0.4 nm-5 nm)

196 at different pressures (0.01-0.2 MPa). It could be seen that the excess adsorption amount was divided

197 into three stages with the increase of the pore size of the graphite slit model: 0.4-0.7 nm, 0.7-1.4 nm,

198 and 1.4-5 nm. in the first stage (0.4-0.7 nm), the excess oxygen physisorption amount decreased rapidly.

199 In the second stage (0.7-1.4 nm), the excess oxygen physisorption decreased slowly. In the third stage

200 (1.4-5 nm), the excess oxygen physisorption amount was kept constant. the trend of excess oxygen

201 physisorption amount was the same for each pressure in the range of 0.01 MPa-0.2 MPa.

202 Figure 6(b) shows the rate of the increasing of the excess oxygen physisorption in different pore

203 sizes with increasing pressure at 298 K. When the pressure was increased from 0.01 MPa to 0.1 MPa,

204 the increment of excess oxygen physisorption in each pore size (mean values of 79% and 47%,

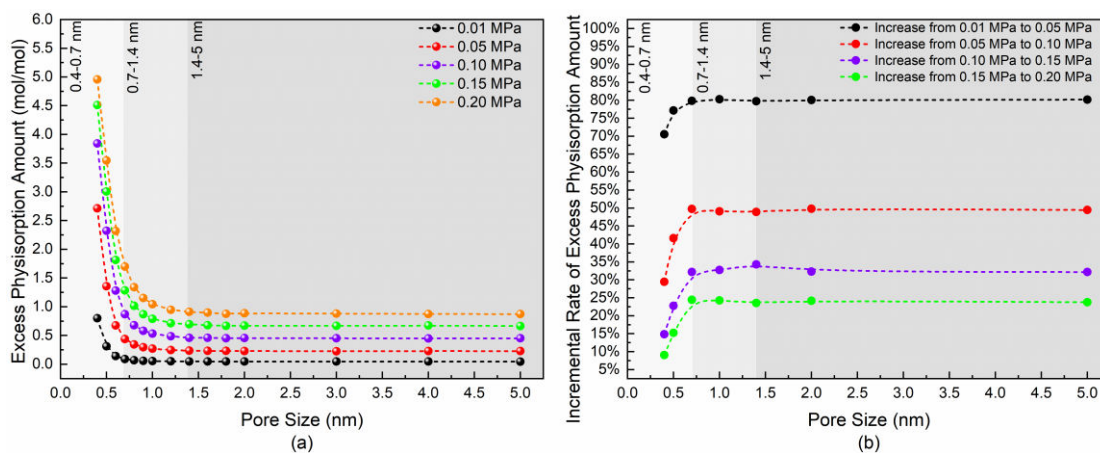
205 respectively) was greater than the increase in pressure from 0.1 MPa to 0.2 MPa (mean values of 31%

206 and 22%, respectively). Similarly, the rate of reduction of excess oxygen physisorption in each pore

207 size for a pressure reduction of 0.01 MPa from 0.1 MPa was greater than that for a pressure reduction

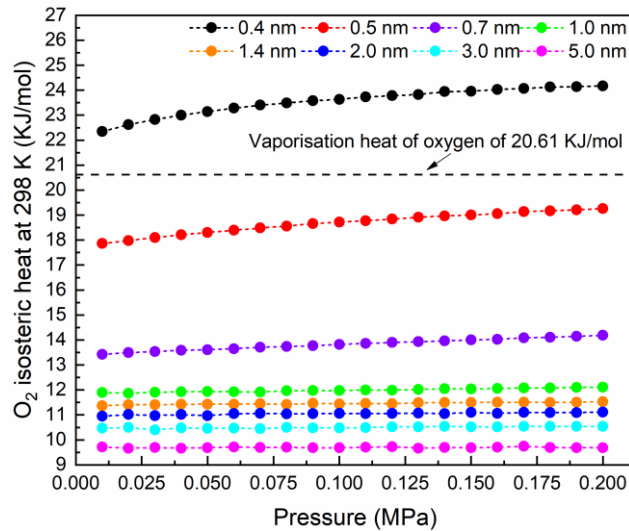
208 from 0.2 MPa to 0.1 MPa. Therefore the excess oxygen physisorption was vulnerable to pressure

209 changes when the pressure was below 0.1 MPa. And the rate of change of oxygen in pores below 0.7
 210 nm was lower than that in pores above 0.7 nm under the same pressure variation. Therefore, the excess
 211 oxygen physisorption in the pores below 0.7 nm was less affected by the pressure change than the other
 212 pores.



213
 214 Figure 6 Excess oxygen physisorption at 298 K for different pore sizes at different pressures (0.01 MPa
 215 to 0.2 MPa) (a), incremental ratio of excess physisorption amount with increasing pressure(b).

216 Figure 7 shown the O_2 isosteric heat at 298 K for different pore sizes at different pressures (0.01
 217 MPa to 0.2 MPa). it could be seen that the increasing in O_2 isosteric heat with the increase in pressure
 218 was small (1.83 KJ/mol). The O_2 isosteric heat is affected by the potential energy of the interaction
 219 between oxygen and graphite surface. The value of O_2 isosteric heat was the value of the physisorption
 220 heat of oxygen in coal pores. In general, the physisorption heat of oxygen was close to the vaporization
 221 heat of oxygen of 20.61 KJ/mol. The physisorption heats for oxygen in 0.4 nm pores were all higher
 222 than 20.61 KJ/mol, while the others were lower than 20.61 KJ/mol. The physisorption heat decreased
 223 continuously with the increase of the pore, mainly due to the decreasing of the potential energy of the
 224 interaction between oxygen and coal pore surface.



225

226 Figure 7 O₂ isosteric heat at 298 K for different pore sizes at different pressures (0.01 MPa to 0.2 MPa)

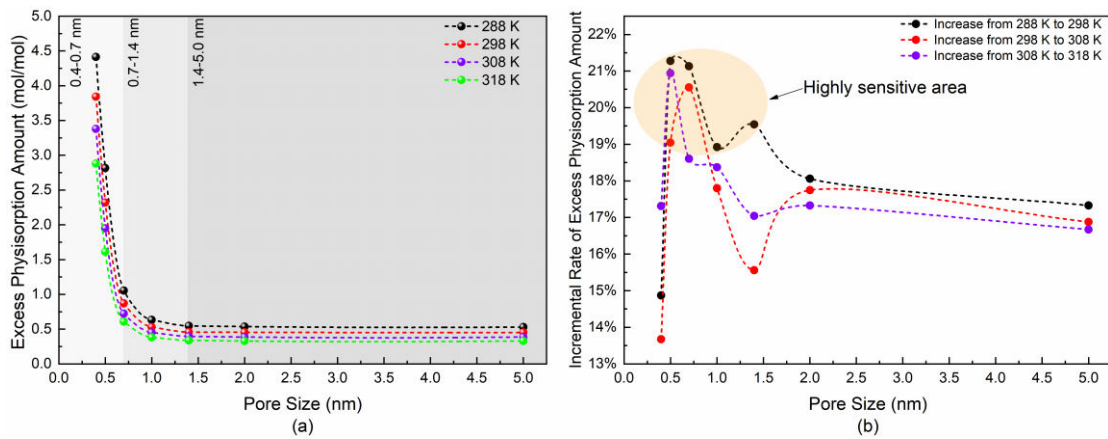
227

228 3.3 Effect of temperature on the physisorption of oxygen in different size pores

229 Figure 8(a) shows the excess oxygen physisorption amount at 0.1 MPa for different pore sizes at
 230 different temperatures (288 K to 318 K). It could be seen that the excess oxygen physisorption amount
 231 in the pores of each size was decreasing as the temperature increased. The tendency of the change of
 232 the excess oxygen physisorption amount with the increasing pore size at different temperatures showed
 233 the same tendency as that of the oxygen density change analyzed previously. However, the tendency of
 234 the incremental change in excess oxygen physisorption amount with increasing temperature was
 235 different from the tendency of the change in excess oxygen physisorption amount with increasing
 236 pressure, as shown in Figure 8(b). The temperature sensitivity of excess oxygen physisorption amount
 237 in pores above 0.4 nm and 1.4 nm was relatively lower, and the decreasing rate of excess oxygen
 238 physisorption amount with increasing temperature was less than 19%. The temperature sensitivity of
 239 excess oxygen physisorption amount in 0.5-1.4 nm pores was higher, and the decrease rate of excess
 240 oxygen physisorption amount with the increasing temperature was more than 19%.

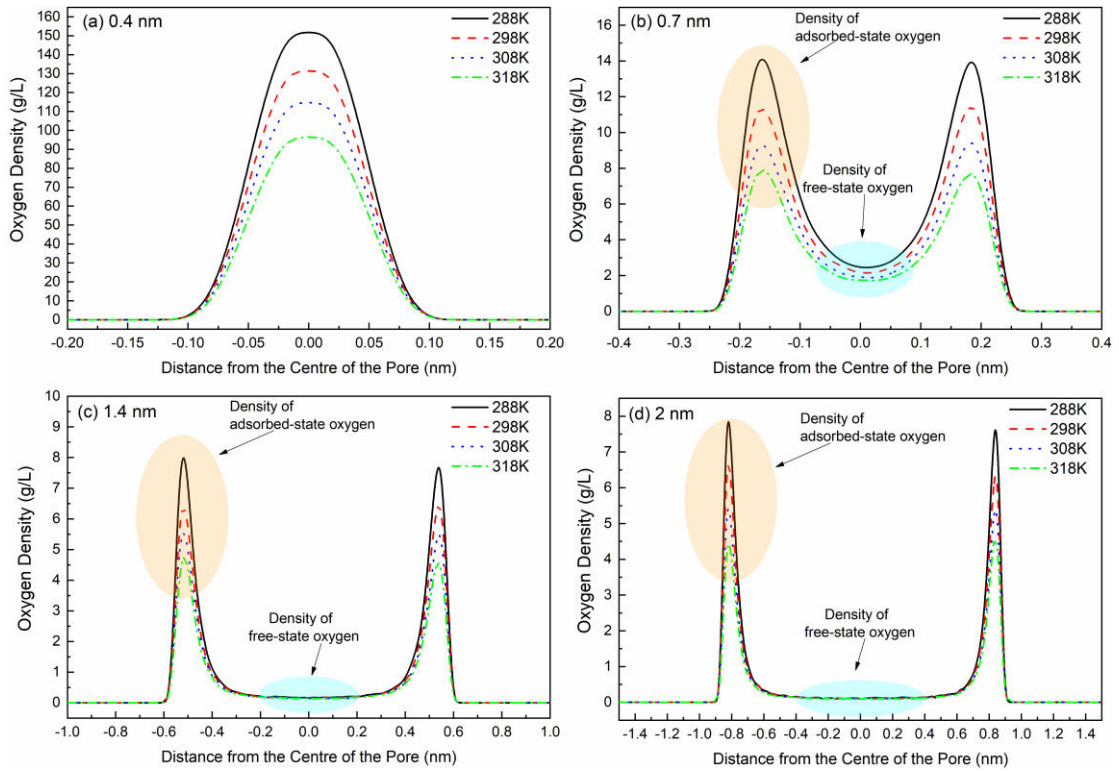
241 The above analysis showed that both the distribution of excess oxygen physisorption amount and

242 oxygen density were influenced by the potential energy of the interaction between oxygen and coal
 243 pore surface. The excess oxygen physisorption amount in micropores (below 2 nm) decreased with the
 244 increasing micropore size for different temperatures (288 to 318 K) and pressures (0.01 to 0.2 MPa),
 245 and the excess oxygen physisorption amount in small pores (2-5 nm) did not change with the pore size.



246
 247 Fig. 8 Excess oxygen physisorption amount at 0.1 MPa for different pore sizes at different temperatures
 248 (288 K to 318 K) (a), reduction rate of excess physisorption amount with increasing temperature (b) .

249 Figure 9 shown the variation of oxygen density with temperature for different pore sizes at
 250 different temperatures (288 K to 318 K) at 0.1 MPa. As shown in Figure 9(a), there was only one layer
 251 of adsorbed-state oxygen in the 0.4 nm pore, and the density of adsorbed-state oxygen decreased with
 252 the increasing of temperature, in which the density of adsorbed-state oxygen in the central part of the
 253 pore decreased the most. As shown in Figure 9(b)-(d), there were two layers of adsorbed-state oxygen,
 254 and also the density of adsorbed-state oxygen decreased with the increasing temperature, but the larger
 255 the pores the smaller the decreasing of the density of adsorbed-state oxygen. In the 0.7 nm pore, the
 256 density of free-state oxygen decreased with the increasing temperature. While in the 1.4 nm and 2 nm
 257 pores, the density of free-state oxygen did not change with the increasing temperature, but the amount
 258 of free-state oxygen kept increasing with the increasing pore volume.

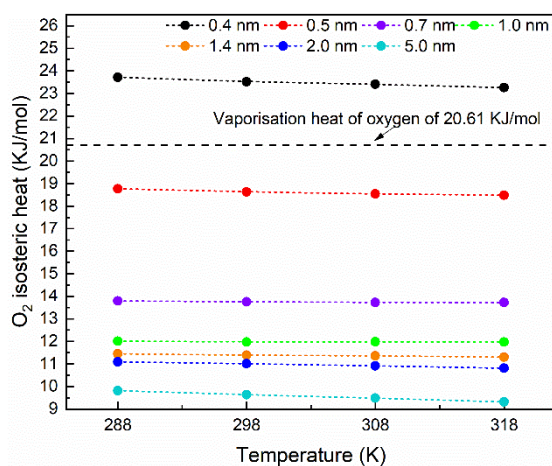


259

260 Figure 9 Variation of oxygen density with temperature at 0.1MPa in pores of different sizes

261 Figure 10 shown that the O_2 isosteric heat for different pore sizes at different temperatures (288 K
 262 to 318 K) at 0.1 MPa. It could be seen that the values of the physisorption heat for each pore size were
 263 the same as the magnitude of the physisorption heat for each pore affected by pressure. However, O_2
 264 isosteric heat decreased with the increasing of temperature (0.46 KJ/mol), so it was considered that the
 265 temperature change had less effect on O_2 isosteric heat. While in Figure 6, the excess oxygen
 266 physisorption amount and O_2 isosteric heat increased with the increasing pressure, while the excess
 267 oxygen physisorption amount and O_2 isosteric heat decreased with the increasing temperature, so the
 268 O_2 isosteric heat was related to the potential energy and also to the excess oxygen physisorption
 269 amount. As shown in Figures 5 and 9, the ratio of the amount of free oxygen to the physisorption
 270 energy was increasing with the increasing pore size, which resulted in the reduction of O_2 isosteric heat
 271 with the increasing pore size. Therefore, oxygen physisorption heat in coal pores is the result of the
 272 combined effect of potential energy, excess oxygen physisorption and the amount of free-state oxygen.

273



274

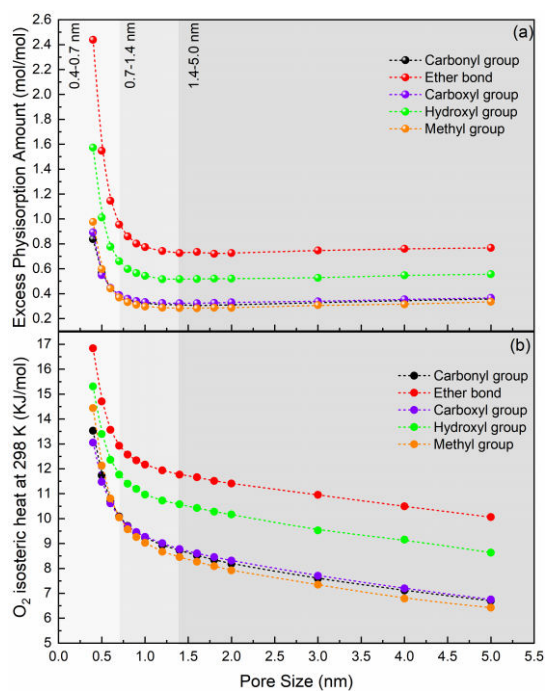
275 Figure 10 O₂ isosteric heat at 0.1 MPa for different pore sizes at different temperatures (288 K to 318
276 K).

277 3.4 Effect of temperature on the physisorption of oxygen in different size pores

278 In order to investigate the effect of different groups in the coal pore on the oxygen physisorption,
279 the physisorption characteristics of the modified graphite slits (Figure 2) for oxygen were analyzed.
280 Figure 10 shown the excess physisorption and isosteric heat of oxygen in graphite slits modified with
281 different groups at 298 K and 0.1 MPa. As shown in Fig. 11(a), the excess oxygen physisorption was
282 divided into three stages as shown in Figure 6(a), but there was a small increase in the excess oxygen
283 physisorption in the modified graphite slit pores between 2.0 and 5.0 nm. The excess oxygen
284 physisorption was higher in the ether-bonded graphite pores, followed by the hydroxyl graphite pores,
285 and the carboxyl, carbonyl and methyl graphite pores were the least.

286 As shown in Figure 11(b), the O₂ isosteric heat continuously decreased with increasing pore size,
287 with faster decreasing rate before 0.7 nm, low decreasing rate between 0.7-1.4 nm, and linear
288 decreasing between 1.4-5.0 nm, which was related to the potential energy of oxygen interaction with
289 graphite surface and the energy of adsorbed-state oxygen analyzed in the previous section. The highest
290 O₂ isosteric heat values were found for the ether-bonded graphite slit pores, followed by the hydroxyl

291 graphite slit pores, and the smallest O₂ isosteric heat for the graphite slit pores of methyl, carboxyl and
 292 carbonyl groups, and the values in the different size pores remained essentially the same. Table 2
 293 shown the adsorption parameters of oxygen near different functional groups, the absolute values of
 294 adsorption energy of hydroxyl and ether bonds with oxygen are higher (12.5120 KJ/mol and 12.3991
 295 KJ/mol) and the absolute values of adsorption energy of the methyl, carboxyl and carbonyl groups with
 296 oxygen were lower (7.7242 KJ/mol, 9.0484 KJ/mol and 10.6515 KJ/ mol), which was consistent with
 297 the O₂ isosteric heat . It indicates that the hydroxyl and ether bond groups are strong for oxygen
 298 physisorption and the methyl, carboxyl and carbonyl groups are weak for oxygen physisorption.



299
 300 Figure 11 Physical adsorption of oxygen (a) and isosteric heat (b) in graphite slit pores modified by
 301 different groups at 298 K and 0.1 MPa.

302 Table 2 Adsorption parameters of oxygen on each group

FG _s	Methyl	Hydroxyl	Ether bond	Carbonyl	Carboxyl
ΔE (KJ/mol)	-7.7242	-12.5120	-12.3991	-10.6515	-9.0484

d_a (nm)	0.2938	0.2394	0.332	0.3074	0.3075
------------	--------	--------	-------	--------	--------

303

304 **4 Conclusion**

305 In this study, the parameters of oxygen physisorption density, physisorption amount and
306 physisorption heat in graphite slit models of different sizes were calculated using GCMC method, and
307 the effect of oxygen physisorption in coal pores by pore size, temperature, pressure and each group was
308 analyzed, and the following conclusions were drawn.

309 (1) Due to the effect of the potential energy of the interaction between oxygen and coal pore
310 surface, the changes of oxygen physisorption density and excess physisorption amount in coal pores
311 with the increasing of pore size were divided into three stages, the first stage (0.4-0.7 nm) was the
312 rapidly decreasing stage; the second stage (0.7-1.4 nm) was the slowly decreasing stage; the third stage
313 (1.4 nm-5 nm) was the stable stage with different temperature (288-318 K), different pressure (0.01-0.2
314 MPa), the graphite slit modified by different groups behaved in the same way.

315 (2) The excess oxygen physisorption in coal pores increased with the increasing pressure and
316 decreased with the increasing temperature. The increasing rate of excess oxygen physisorption with
317 increasing pressure (0.01-0.2 MPa) was 22%-79%, and the decreasing rate of excess oxygen
318 physisorption with increasing temperature (288-318 K) was 13%-20%, and the excess oxygen
319 physisorption was more sensitive to the change of pressure. The pressure was below 0.1 MPa, and the
320 amount of excess oxygen physisorption in pores above 1 nm was highly affected by pressure. The
321 excess oxygen physisorption amount in 0.5-1.4 nm pores was highly affected by temperature.

322 (3) Under different temperatures (288-318 K) and pressures (0.01-0.2 MPa), the continuous
323 decreasing of potential energy and the continuous increasing of free-state oxygen with increasing pore

324 size, which led to the decreasing of physisorption heat with increasing pore size. The physisorption
325 heat of oxygen in the coal pores increased with the increasing pressure and decreased with the
326 increasing temperature.

327 (4) Simulated data of excess physisorption and physisorption heat of oxygen at 298 K and 0.1
328 MPa for graphite slit models with different groups showed strong physisorption of oxygen by hydroxyl
329 and ether bonds versus methyl, carboxyl and carbonyl groups.

330

331 **CRedit authorship contribution statement**

332 **Cheng Gang:** Conceptualization, Formal analysis, Writing - original draft, Writing - review &
333 editing, Molecular simulation; **Tan Bo:** Conceptualization, Investigation, Supervision, Funding
334 acquisition; **Wang Feiran:** Supervision, Writing - review & editing.

335 **Declaration of competing interest**

336 The authors declare that they have no known competing financial interests or personal
337 relationships that could have appeared to influence the work reported in this paper.

338 **Acknowledgement**

339 Financial support was provided by the National Nature Science Foundation of China (51864045
340 and 51774291).

341

342 **References**

343 [1] Tan B, Wei H, Xu B, Zhao H, Shao Z. Investigation on the effect of transition metal chloride
344 on anthracite combustion. Fuel 2020;264. <https://doi.org/10.1016/j.fuel.2019.116796>

- 345 [2] B.Petroleum. BP Energy Outlook: 2020 edition; BP Amoco. 2020.
346 <https://www.bp.com/en/global/corporate/energy-economics/energy-outlook/demand-by-fuel/c>
347 [oal.html](https://www.bp.com/en/global/corporate/energy-economics/energy-outlook/demand-by-fuel/c)
- 348 [3] Ma L, Yu W, Ren L, Qin X, Wang Q. Micro-characteristics of low-temperature coal oxidation
349 in CO₂/O₂ and N₂/O₂ atmospheres. Fuel 2019;246:259-67.
350 <https://doi.org/10.1016/j.fuel.2019.02.073>
- 351 [4] Arisoy A, Beamish B. Reaction kinetics of coal oxidation at low temperatures. Fuel
352 2015;159:412-7. <https://doi.org/10.1016/j.fuel.2015.06.054>
- 353 [5] Beamish BB, Barakat MA, St George JD. Adiabatic testing procedures for determining the
354 self-heating propensity of coal and sample ageing effects. Thermochimica Acta
355 2000;362(1-2):79-87. [https://doi.org/10.1016/s0040-6031\(00\)00588-8](https://doi.org/10.1016/s0040-6031(00)00588-8)
- 356 [6] Zhang R, Liu S, Wang Y. Fractal evolution under in situ pressure and sorption conditions for
357 coal and shale. Scientific Reports 2017;7(1):1-11.
358 <https://doi.org/10.1038/s41598-017-09324-9>
- 359 [7] Mathews JP, Chaffee AL. The molecular representations of coal – A review. Fuel
360 2012;96:1-14. <https://doi.org/10.1016/j.fuel.2011.11.025>
- 361 [8] Dombrowski RJ, Hyduke DR, Lastoskie CM. Pore size analysis of activated carbons from
362 argon and nitrogen porosimetry using density functional theory. Langmuir
363 2000;16(11):5041-50. <https://doi.org/10.1021/la990827a>
- 364 [9] Zhu J, He F, Zhang Y, Zhang R, Zhang B. Fractal Analysis in Pore Size Distributions of
365 Different Bituminous Coals. Sci Rep 2019;9(1):18162.
366 <https://doi.org/10.1038/s41598-019-54749-z>

- 367 [10] Liu Y, Zhu Y, Liu S, Li W. A hierarchical methane adsorption characterization through a
368 multiscale approach by considering the macromolecular structure and pore size distribution.
369 Marine and Petroleum Geology 2018;96:304-14.
370 <https://doi.org/10.1016/j.marpetgeo.2018.06.006>
- 371 [11] Wojtacha-Rychter K, Smolinski A. A study of dynamic adsorption of propylene and ethylene
372 emitted from the process of coal self-heating. Sci Rep 2019;9(1):18277.
373 <https://doi.org/10.1038/s41598-019-54831-6>
- 374 [12] Tan B, Cheng G, Zhu X, Yang X. Experimental Study on the Physisorption Characteristics of
375 O₂ in Coal Powder are Effected by Coal Nanopore Structure. Scientific Reports
376 2020;10(1):6946. <https://doi.org/10.1038/s41598-020-63988-4>
- 377 [13] Liu Y, Zhu Y, Liu S, Li W, Tang X. Temperature effect on gas adsorption capacity in different
378 sized pores of coal: Experiment and numerical modeling. Journal of Petroleum Science and
379 Engineering 2018;165:821-30. <https://doi.org/10.1016/j.petrol.2018.03.021>
- 380 [14] Zhang J, Liu K, Clennell MB, Dewhurst DN, Pervukhina M. Molecular simulation of CO₂-
381 CH₄ competitive adsorption and induced coal swelling. Fuel 2015;160:309-17.
382 <https://doi.org/10.1016/j.fuel.2015.07.092>
- 383 [15] Yu S, Bo J, Fengjuan L. Competitive adsorption of CO₂/N₂/CH₄ onto coal vitrinite
384 macromolecular: Effects of electrostatic interactions and oxygen functionalities. Fuel
385 2019;235:23-38. <https://doi.org/10.1016/j.fuel.2018.07.087>
- 386 [16] Bai Y, Lin H-F, Li S-G, Yan M, Long H. Molecular simulation of N₂ and CO₂ injection into a
387 coal model containing adsorbed methane at different temperatures. Energy 2021;219.
388 <https://doi.org/10.1016/j.energy.2020.119686>

- 389 [17] Meng J, Niu J, Meng H, Xia J, Zhong R. Insight on adsorption mechanism of coal molecules
390 at different ranks. *Fuel* 2020;267. <https://doi.org/10.1016/j.fuel.2020.117234>
- 391 [18] Loi QK, Prasetyo L, Tan J, Do DD, Nicholson D. Wedge pore modelling of gas adsorption in
392 activated carbon: Consistent pore size distributions. *Carbon* 2020;166:414-26.
393 <https://doi.org/10.1016/j.carbon.2020.05.035>
- 394 [19] Chen C, Hu W, Sun J, Li W, Song Y. CH₄ adsorption and diffusion in shale pores from
395 molecular simulation and a model for CH₄ adsorption in shale matrix. *International Journal of*
396 *Heat and Mass Transfer* 2019;141:367-78.
397 <https://doi.org/10.1016/j.ijheatmasstransfer.2019.06.087>
- 398 [20] Yu S, Bo J, Wu L. Molecular simulation of CH₄/CO₂/H₂O competitive adsorption on low
399 rank coal vitrinite. *Phys Chem Chem Phys* 2017;19(27):17773-88.
400 <https://doi.org/10.1039/c7cp02993d>
- 401 [21] Yutong F, Yu S. CO₂-adsorption promoted CH₄-desorption onto low-rank coal vitrinite by
402 density functional theory including dispersion correction (DFT-D3). *Fuel* 2018;219:259-69.
403 <https://doi.org/10.1016/j.fuel.2018.01.127>
- 404 [22] Cornette V, Villarroel-Rocha J, Sapag K, Delgado Mons R, Toso JP, López RH. Insensitivity
405 in the pore size distribution of ultramicroporous carbon materials by CO₂ adsorption. *Carbon*
406 2020;168:508-14. <https://doi.org/10.1016/j.carbon.2020.07.011>
- 407 [23] Zhang L, Xiao Y, Chung T-S, Jiang J. Mechanistic understanding of CO₂-induced
408 plasticization of a polyimide membrane: A combination of experiment and simulation study.
409 *Polymer* 2010;51(19):4439-47. <https://doi.org/10.1016/j.polymer.2010.07.032>

- 410 [24] Sugiura H, Kondo H, Higuchi K, Arai S, Hamaji R, Tsutsumi T, et al. Reaction science of
411 layer-by-layer thinning of graphene with oxygen neutrals at room temperature. Carbon
412 2020;170:93-9. <https://doi.org/10.1016/j.carbon.2020.07.052>
- 413 [25] Zhou Q, Ju W, Yong Y, Su X, Li X, Fu Z, et al. Effect of H-vacancy defect on the adsorption
414 of CO and NO on graphane: A DFT study. Applied Surface Science 2017;420:720-5.
415 <https://doi.org/10.1016/j.apsusc.2017.05.234>
- 416 [26] Dang Y, Zhao L, Lu X, Xu J, Sang P, Guo S, et al. Molecular simulation of CO₂/CH₄
417 adsorption in brown coal: Effect of oxygen-, nitrogen-, and sulfur-containing functional
418 groups. Applied Surface Science 2017;423:33-42.
419 <https://doi.org/10.1016/j.apsusc.2017.06.143>
- 420 [27] Ji W-M, Zhang L-W, Liew KM. Understanding interfacial interaction characteristics of carbon
421 nitride reinforced epoxy composites from atomistic insights. Carbon 2021;171:45-54.
422 <https://doi.org/10.1016/j.carbon.2020.08.067>
- 423 [28] Tang Y, Liu Z, Dai X, Yang Z, Chen W, Ma D, et al. Theoretical study on the Si-doped
424 graphene as an efficient metal-free catalyst for CO oxidation. Applied Surface Science
425 2014;308:402-7. <https://doi.org/10.1016/j.apsusc.2014.04.189>
- 426 [29] Chong L, Sanguinito S, Goodman AL, Myshakin EM. Molecular characterization of carbon
427 dioxide, methane, and water adsorption in micropore space of kerogen matrix. Fuel 2021;283.
428 <https://doi.org/10.1016/j.fuel.2020.119254>
- 429 [30] Wang K, Zhang B, Kang T. Effect of Geological Depths on CH₄ Adsorption, Diffusion, and
430 Swelling in Kaolinite by Molecular Simulations. Energy & Fuels 2020;34(2):1620-6.
431 <https://doi.org/10.1021/acs.energyfuels.9b03859>

- 432 [31] Liu Y, Zhu Y, Li W, Xiang J, Wang Y, Li J, et al. Molecular simulation of methane adsorption
433 in shale based on grand canonical Monte Carlo method and pore size distribution. Journal of
434 Natural Gas Science and Engineering 2016;30:119-26.
435 <https://doi.org/10.1016/j.jngse.2016.01.046>
- 436 [32] Kanca A, Dodd M, Reimer JA, Uner D. Following the structure and reactivity of Tuncbilek
437 lignite during pyrolysis and hydrogenation. Fuel Processing Technology 2016;152:266-73.
438 <https://doi.org/10.1016/j.fuproc.2016.06.014>
- 439 [33] Kuenzer C, Stracher GB. Geomorphology of coal seam fires. Geomorphology
440 2012;138(1):209-22. <https://doi.org/10.1016/j.geomorph.2011.09.004>
- 441 [34] Zhou Y, Sun W, Chu W, Liu X, Jing F, Xue Y. Theoretical insight into the enhanced CH₄
442 desorption via H₂O adsorption on different rank coal surfaces. Journal of Energy Chemistry
443 2016;25(4):677-82. <https://doi.org/10.1016/j.jechem.2016.04.011>
- 444 [35] Diao R, Fan C, Do DD, Nicholson D. On the adsorbate restructuring induced hysteresis of
445 simple gas adsorption in slit micropores. Chemical Engineering Journal 2016;290:381-90.
446 <https://doi.org/10.1016/j.cej.2016.01.072>
- 447 [36] Peng X, Jin Q. Ideal adsorbed solution theory, two-dimensional equation of state, and
448 molecular simulation for separation of H₂/N₂/O₂/CH₄/CO in graphite nanofiber and C-60
449 intercalated graphite. Separation and Purification Technology 2020;237.
450 <https://doi.org/10.1016/j.seppur.2019.116369>
- 451 [37] Pitakbunkate T, Blasingame TA, Moridis GJ, Balbuena PB. Phase Behavior of
452 Methane-Ethane Mixtures in Nanopores. Industrial & Engineering Chemistry Research
453 2017;56(40):11634-43. <https://doi.org/10.1021/acs.iecr.7b01913>

- 454 [38] Cai Y, Liu D, Yao Y, Li J, Liu J. Fractal Characteristics of Coal Pores Based on Classic
455 Geometry and Thermodynamics Models. *Acta Geologica Sinica-English Edition*
456 2011;85(5):1150-62. <https://doi.org/10.1111/j.1755-6724.2011.00247.x>
- 457 [39] Zhou S, Liu D, Cai Y, Yao Y. Effects of the coalification jump on the petrophysical properties
458 of lignite, subbituminous and high-volatile bituminous coals. *Fuel* 2017;199:219-28.
459 <https://doi.org/10.1016/j.fuel.2017.02.092>
- 460 [40] Song D, Ji X, Li Y, Zhao H, Song B, He K. Heterogeneous development of micropores in
461 medium-high rank coal and its relationship with adsorption capacity. *International Journal of*
462 *Coal Geology* 2020;226. <https://doi.org/10.1016/j.coal.2020.103497>
- 463 [41] Shan Ca, Zhang T, Liang X, Shu D, Zhang Z, Wei X, et al. Effects of nano-pore system
464 characteristics on CH₄ adsorption capacity in anthracite. *Frontiers of Earth Science*
465 2018;13(1):75-91. <https://doi.org/10.1007/s11707-018-0712-1>
- 466 [42] Wang B, Chen W, Fu H, Qu X, Zheng S, Xu Z, et al. Comparison of adsorption isotherms of
467 single-ringed compounds between carbon nanomaterials and porous carbonaceous materials
468 over six-order-of-magnitude concentration range. *Carbon* 2014;79:203-12.
469 <https://doi.org/10.1016/j.carbon.2014.07.061>
- 470 [43] Li Q, Zhao C, Chen X, Wu W, Lin B. Properties of char particles obtained under O₂/N₂ and
471 O₂/CO₂ combustion environments. *Chemical Engineering and Processing: Process*
472 *Intensification* 2010;49(5):449-59. <https://doi.org/10.1016/j.cep.2010.03.007>
- 473 [44] Liu Y, Fu P, Bie K, Gong Y, Xu T. The intrinsic reactivity of coal char conversion compared
474 under different conditions of O₂/CO₂, O₂/H₂O and air atmospheres. *Journal of the Energy*
475 *Institute* 2020;93(5):1883-91. <https://doi.org/10.1016/j.joei.2020.04.003>

- 476 [45] Liu Y, Fu P, Zhang B, Yue F, Zhou H, Zheng C. Study on the surface active reactivity of coal
477 char conversion in O₂/CO₂ and O₂/N₂ atmospheres. Fuel 2016;181:1244-56.
478 <https://doi.org/10.1016/j.fuel.2016.01.077>
- 479 [46] Yoshiie R, Onda M, Ueki Y, Naruse I. Oxygen chemisorption and low-temperature oxidation
480 behaviors of sub-bituminous coal. Journal of Thermal Science and Technology
481 2019;14(1):JTST0005-JTST. <https://doi.org/10.1299/jtst.2019jtst0005>
- 482 [47] Zhao P, Zhang G, Sun Y, Xu Y. A review of oxygen removal from oxygen-bearing coal-mine
483 methane. Environmental Science and Pollution Research 2017;24(18):15240-53.
484 <https://doi.org/10.1007/s11356-017-8916-6>
- 485 [48] Zhong XX, Wang DM, Lu W, Xin HH. Oxygen Physisorption Characteristics of Coal.
486 Materials Science Forum 2011;704-705:897-902.
487 <https://doi.org/10.4028/www.scientific.net/MSF.704-705.897>
- 488 [49] Lv X, Liang X, Xu P, Chen L. A numerical study on oxygen adsorption in porous media of
489 coal rock based on fractal geometry. R Soc Open Sci 2020;7(2):191337.
490 <https://doi.org/10.1098/rsos.191337>
- 491 [50] Xin H-h, Wang D-m, Dou G-l, Qi X-y, Xu T, Qi G-s. The Infrared Characterization and
492 Mechanism of Oxygen Adsorption in Coal. Spectroscopy Letters 2014;47(9):664-75.
493 <https://doi.org/10.1080/00387010.2013.833940>
- 494 [51] Cao J, Liang Y, Masuda Y, Koga H, Tanaka H, Tamura K, et al. Molecular simulation of CH₄
495 adsorption behavior in slit nanopores: Verification of simulation methods and models. Aiche
496 Journal 2019;65(11). <https://doi.org/10.1002/aic.16733>

- 497 [52] Dehghani M, Asghari M, Ismail AF, Mohammadi AH. Molecular dynamics and Monte Carlo
498 simulation of the structural properties, diffusion and adsorption of poly (amide-6-b-ethylene
499 oxide)/Faujasite mixed matrix membranes. *Journal of Molecular Liquids* 2017;242:404-15.
500 <https://doi.org/10.1016/j.molliq.2017.07.034>
- 501 [53] Chen Z, Qiu H, Hong Z, Wang G. Molecular dynamics simulation of a lignite structure
502 simplified model absorbing water. *Molecular Simulation* 2019;46(1):71-81.
503 <https://doi.org/10.1080/08927022.2019.1674851>
- 504 [54] Nagar H, Vadthya P, Prasad NS, Sridhar S. Air separation by facilitated transport of oxygen
505 through a Pebax membrane incorporated with a cobalt complex. *RSC Advances*
506 2015;5(93):76190-201. <https://doi.org/10.1039/c5ra10755e>
- 507 [55] Prasetyo L, Tan S, Zeng Y, Do DD, Nicholson D. An improved model for N₂ adsorption on
508 graphitic adsorbents and graphitized thermal carbon black—The importance of the anisotropy
509 of graphene. *The Journal of Chemical Physics* 2017;146(18).
510 <https://doi.org/10.1063/1.4982926>
- 511 [56] Delhommelle J, MilliÉ P. Inadequacy of the Lorentz-Berthelot combining rules for accurate
512 predictions of equilibrium properties by molecular simulation. *Molecular Physics*
513 2001;99(8):619-25. <https://doi.org/10.1080/00268970010020041>
- 514 [57] Rafati AA, Hashemianzadeh SM, Nojini ZB. Effect of the adsorption of oxygen on electronic
515 structures and geometrical parameters of armchair single-wall carbon nanotubes: a density
516 functional study. *J Colloid Interface Sci* 2009;336(1):1-12.
517 <https://doi.org/10.1016/j.jcis.2009.03.021>

- 518 [58] Liu X-Q, He X, Qiu N-X, Yang X, Tian Z-Y, Li M-J, et al. Molecular simulation of CH₄, CO₂,
519 H₂O and N₂ molecules adsorption on heterogeneous surface models of coal. Applied Surface
520 Science 2016;389:894-905. <https://doi.org/10.1016/j.apsusc.2016.08.021>
- 521 [59] Hao S, Wen J, Yu X, Chu W. Effect of the surface oxygen groups on methane adsorption on
522 coals. Applied Surface Science 2013;264:433-42. <https://doi.org/10.1016/j.apsusc.2012.10.040>
- 523 [60] Zhang Z, Li Z, Li J. Computational study of adsorption and separation of CO₂, CH₄, and N₂
524 by an rht-type metal-organic framework. Langmuir 2012;28(33):12122-33.
525 <https://doi.org/10.1021/la302537d>
- 526 [61] Klymenko VE, Rozenbaum VM. Orientational behaviour of O₂ molecules: interplay of van
527 der Waals, quadrupole and magnetodipole interactions. Molecular Physics
528 2009;101(18):2855-9. <https://doi.org/10.1080/00268970310001598731>
- 529